



Article

# Analysis of Unsteady Pressure Fluctuation in a Semi-Open Cutting Pump

Weidong Cao <sup>1,2,\*</sup> , Jiayu Mao <sup>1</sup> and Wei Li <sup>2,\*</sup> 

<sup>1</sup> Research Institute of Fluid Engineering Technology, Jiangsu University, Zhenjiang 212013, China; m jy1006a@163.com

<sup>2</sup> China National Research Center of Pumps, Jiangsu University, Zhenjiang 212013, China

\* Correspondence: cwd@ujs.edu.cn (W.C.); lwjiangda@ujs.edu.cn (W.L.); Tel.: +86-1395-281-6468 (W.C.); +86-1377-555-4729-9 (W.L.)

Received: 16 June 2020; Accepted: 13 July 2020; Published: 15 July 2020



**Abstract:** In order to understand the pressure fluctuation characteristics of a semi-open cutting pump, the three-dimensional unsteady flow fields were calculated. External and internal flow characteristics of four schemes with different relative angles between the rotary cutter and the impeller were studied. The pressure fluctuations in the lower plate, the upper plate, the clearance between the rotary cutter and the fixed cutter, the first section in volute and nearby parts of the tongue were all analyzed, which are all the places that pressure distributions are greatly affected by the static and dynamic interaction, and at the same time, the force on the impeller was also analyzed. The results show that the fluctuations at different positions change periodically; the main frequency is blade frequency. The amplitude of pressure fluctuation decreases from near the rotating part to far away, from near the tongue to far from the tongue. Due to the influence of both impeller and rotary cutter, the pressure fluctuation on the lower plate is the largest. The pressure fluctuation is affected by flow rate, the larger the flow rate greater the pressure fluctuation. The radial and axial forces of the impeller change periodically with time, and the number of wave peaks and wave valleys is the same as the number of blades.

**Keywords:** cutting pump; unsteady pressure; rotary cutter; radial force; axial force

## 1. Introduction

Sewage pumps are widely used in municipal engineering, environmental protection engineering, power industrial engineering, sewage treatment station, mining, metallurgy, medical and health services and many other industries. Compared with traditional sewage pumps, the semi-open cutting pump is not easy to be blocked, which can be used to transport sewage, waste water, rainwater and urban domestic water containing solid particles and various fibers. As a kind of rotating machinery, the semi-open submersible cutting pump faces with vibration, noise, operation instability and other problems, these problems are related to the unsteady pressure fluctuations in the pump cavity, namely the axial and radial forces.

Adkins et al. [1] and Barrio et al. [2] studied the radial force distribution of a centrifugal pump rotor through theoretical analysis and numerical calculation. In order to improve the force on the impeller of single blade spiral centrifugal pump, Yuan et al. [3] used a numerical simulation method to calculate the internal flow field of the pump, and the characteristics of pressure pulsation at the outlet of spiral centrifugal pump and the radial force acting on the impeller and volute were obtained. González et al. [4] Barrio et al. [5] Solis et al. [6] studied the radial force characteristics of the impeller and the pressure fluctuation at the tongue under different tongue clearance conditions of a centrifugal pump. It was found that the changes of tongue clearance had a great influence on the radial force

and pressure fluctuation of centrifugal pump. Through numerical calculation and test methods, they studied the radial force of centrifugal pump with different impeller outer diameter, and compared the numerical calculation and test results, Esch [7], José González et al. [8] found that the numerical calculation results were in good agreement with test results. Han et al. [9] studied the pressure fluctuation characteristics caused by unsteady flow in the dynamic and static cascade when the pump was used as the turbine for flowing sediment laden water. Taking the reverse flow of radial guide vane centrifugal pump as the research object, the whole flow channel was divided into structured hexahedron grids. The large eddy simulation (LES) and the mixture multiphase flow model were combined to carry out three-dimension unsteady numerical calculation. The pressure fluctuation under three flow conditions of clear water medium and solid–liquid two-phase medium was monitored. Cao [10] studied the distribution of unsteady pressure in volute type axial flow pump. Wei Li [11] studied the unsteady flow characteristics in a mixed flow pump. For the unsteady flow characteristics inside the mixed flow pump, the external characteristics and internal flow field of the mixed flow pump were calculated by ANSYS CFX software. The distribution of the radial force of the rotor under different flow conditions and the time–domain and frequency–domain response of the pressure fluctuation at different monitoring points were obtained. The influence of different flow conditions on the radial force and pressure fluctuation of the mixed flow pump rotor was analyzed.

The existing researches mainly focus on the pressure fluctuation characteristics of impeller, volute and guide vane of typical centrifugal pumps. The auxiliary structures in a cutting pump can disintegrate solids and prevent the pump from blocking. For the submersible pump with a special structure, such as upper plate, lower plate and rotary cutter with pre-cutting function, the characteristics of internal impeller and imported rotary cutter interacting with the volute, as well as the pressure pulsation and axial and radial force of impeller components, are still lacking systematic research. In this paper, the external characteristics of the cutting pump under different flow conditions are compared and analyzed through numerical simulation and experimental research. Based on the unsteady numerical calculation, the radial force of the rotor at different phases and the pressure fluctuations at different positions under different flow conditions are monitored, and the influence of flow rates changing on the radial force and pressure fluctuation amplitude of the rotor is discussed. The research on the internal flow and unsteady pressure fluctuation of cutting pumps can promote the optimization design, reduce vibration and noise, prevent faults caused by hydraulic radial force, and benefit to the design processes of large-scale sewage cutting pump.

## 2. Physical Model and Numerical Calculation Method

### 2.1. Model Parameters

The structure of the semi-open cutting pump is shown in Figure 1. From top to bottom are motor, volute, upper plate, impeller, lower plate, rotary cutter and fixed cutter. Sewage with fibers, branches and other sundries enters into the pump from the bottom, it will be cut for the first time at the clearance between the rotary cutter and the fixed cutter, then will be cut for the second time at the clearance between the rotary cutter and the lower plate. The upper plate with grooves interacting with the impeller's arc blades forms a triple cut, and the upper plate with grooves interacting with the back blades of the impeller forms a quadruple cut. At last the sewage flows out of the outlet. The main design parameters are as follows: rated flow  $Q_{opt}$  is 90 m<sup>3</sup>/h, head  $H_{opt}$  is 13 m, rotating speed  $n$  is 1480 r/min, and motor power is 7.5 kW. The parameters of the semi-open impeller with back blades are as follows: outside diameter  $D_2$  is 249 mm, outlet width  $b_2$  is 35.8 mm, and blades number  $Z$  is 3. Relevant dimensions of rotary cutter are as follows: hub  $D_3$  is 70 mm, maximum outer diameter  $D_4$  is 138 mm, and blade number  $Z$  is 3. Those shown in Figure 2a–d are impeller, upper plate, lower plate and rotary cutter, respectively. Grooves with certain shape and depth are designed on the upper plate and the lower plate, respectively. There are back blades on the impeller. Four blades with certain inclination angle are arranged on the fixed cutter.

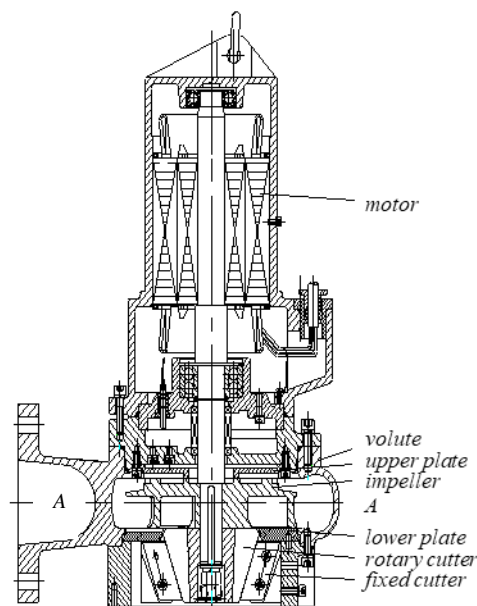


Figure 1. Structure of the pump.

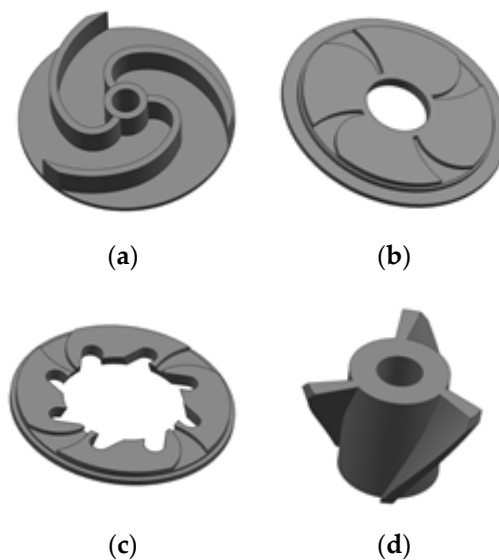
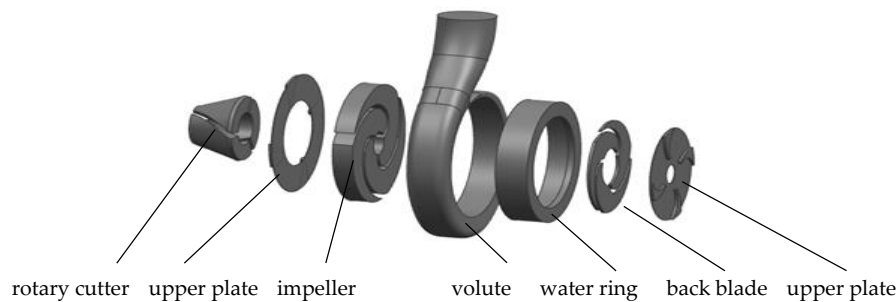


Figure 2. (a) Structure of impeller, (b) upper plate, (c) lower plate and (d) rotary cutter.

## 2.2. Calculation Method and Grid Division

In order to obtain the pressure fluctuation characteristics and the distribution of radial force and axial force in the semi-open submersible cutting pump, the commercial computational fluid dynamics (CFD) software ANSYS CFX 15.0 (ANSYS Inc., Pittsburgh, PA, USA) was used to solve the internal Reynolds averaged equations of three dimensional flow fields. Based on the results of steady calculation, the unsteady internal flow fields of  $0.6Q_{opt}$ ,  $0.8Q_{opt}$ ,  $1.0Q_{opt}$ ,  $1.2Q_{opt}$  and  $1.4Q_{opt}$  were calculated. The standard  $k-\varepsilon$  turbulence model was adopted in the simulation as the model is one of the most widely used models to study the flow field of sewage pumps [12–14]. The rotating parts include rotary cutter, impeller with back blades. The static domain includes inlet extension section, volute, and water ring in volute, lower plate, upper plate and outlet extension section, the whole computational domain is shown in Figure 3. The rotation speed is 1480 r/min; the medium is water and the temperature is 25 degrees centigrade. Frozen rotor is used for the interfaces of impeller and inlet extension section, impeller and upper plate, impeller and lower plate. The interface between the

static and static fields is set to be none. The GGI (grid-grid interface) method with strong compatibility is chosen for the connection of the domain interface. The inlet boundary is set as total pressure of one standard atmospheric pressure,  $1.01325 \times 10^5 \text{ p}_a$ , the outlet boundary is set as mass flow rate, and walls are set to be non-slip. The roughness of the main flow parts such as rotary cutter and impeller is set to be 0.025 mm. In the solver, high resolution is selected for the numerical dispersion method of the convection term in the transport equation. The discretization of the turbulence equation is set as the second-order upwind, the maximum time step is 2000, and the convergence accuracy is  $10^{-5}$ .



**Figure 3.** Whole computational domains.

During unsteady simulation, calculation time step is set to be  $3.37838 \times 10^{-4} \text{ s}$ , which is the time for every three degrees of impeller rotation, and the total calculation time is set to be 0.405405405 s. That is to say, it takes 1200 steps to rotate the impeller for 10 circles. The dynamic and static interface is changed to transient rotor-stator. The convergence accuracy is set to  $10^{-5}$  too, and the maximum iteration is 20, so as to ensure the accuracy and time of calculation. In order to obtain more reliable unsteady calculation results, calculation data of the last four circles are selected for analysis.

To verify the mesh independence, when the number of grid nodes reaches 4.08 million, the head and efficiency tend to be stable, as shown in Figure 4, the number of grids and  $y+$  value in each part are shown in Table 1.

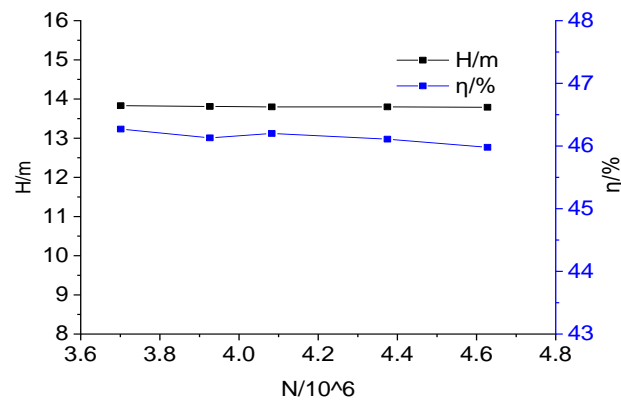


**Figure 4.** Mesh independence analyses.

**Table 1.** Number of grids and  $y+$  value in each area.

Parts	Inlet Extension	Rotary Cutter	Volute	Water Ring in Volute	Impeller and Back Blade	Lower Plate	Upper Plate	Outlet Extension
Number of grids	440,679	737,995	857,656	101,684	1,201,552	181,292	140,444	447,042
$y+$	66.4	85.7	102.3	92.1	95.3	82.5	83.5	75.6

### 2.3. Location of Pressure Pulsation Monitoring Point

Monitoring points are set up at the entrance of the rotary cutter, the clearance between the rotary cutter and the fixed cutter, the groove of the lower and upper plate, the cross-section of the volute,



the impeller outlet and the impeller runner. The locations of the monitoring point are shown in Figure 5. Dynamic and static interaction is the main cause of the pressure fluctuation. The rotary cutter inlet, the rotary cutter and the fixed cutter are mainly within the influence of the rotary cutter. The lower plate, the upper plate and the volute are within the influence of the impeller. Therefore, the above locations are selected as the research objects.

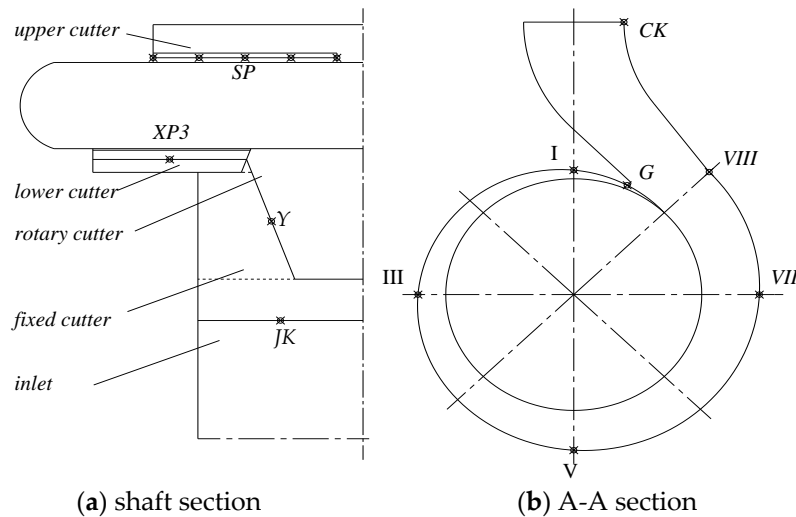


**Figure 5.** Monitoring points position.

As shown in Figure 5a, from the bottom to the top, the monitoring point JK is at the rotary cutter inlet, Y is at the clearance between rotary cutter and fixed cutter, XP is at the groove of lower plate and SP is at the groove of upper plate. As shown in Figure 5b, monitoring points P1, P3, P5, P7, P8 are respectively set at Sections I, III, V, VII and VIII of the volute, G is at the tongue and CK is at the volute outlet.

### 3. Results and Analysis

#### 3.1. Flow Characteristics for Different Relative Angles

As the core part of the submersible cutting pump, the impeller affects the head and efficiency of the pump. Due to the existence of the rotary cutter, the distribution of the flow field in the pump changes, which will affect the head and efficiency of the pump. The experimental pump is of semi-open impeller, the number of impeller blades is three, and the number of rotary cutter blades is three. The impeller and the rotary cutter are cast together. When the rotary cutter rotates 120 degrees, the relative position of the rotary cutter and the impeller coincides. Therefore, 120 degrees relative angle between the rotary cutter and the impeller is taken as the research object here.

##### 3.1.1. External Characteristic Analysis

The performance curve of the pump at different relative angles under  $1.0Q_{opt}$  flow rate is shown in Figure 6. When the relative angle is 20 degrees, 40 degrees, 80 degrees and 100 degrees, it is found that, when the relative angle between the rotary cutter and the impeller is 20 degrees, the head is 13.8 m, and the error rate of the design head which is calculated by  $(13.8 - 13)/13 = 6.15\%$  is the smallest, the efficiency of about 46.2% is relatively acceptable. In general, the efficiency difference of the pump with different angles is small when the relative angle is in the range of 20 to 110 degrees, and the internal flow characteristics are analyzed. Figure 7 is the schemes of rotary cutter and impeller under four different angles.

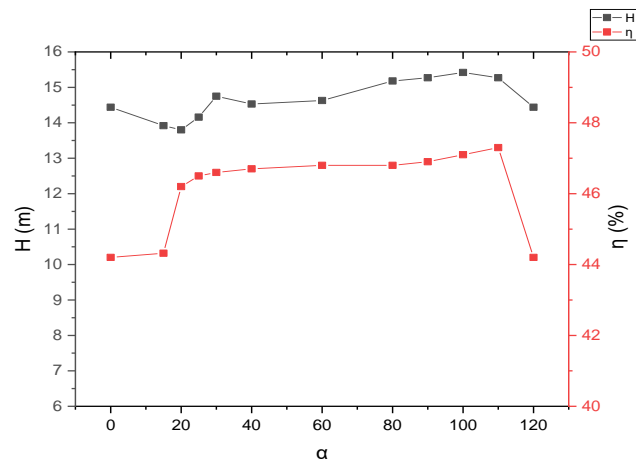


Figure 6. Performance curves under different relative angles.

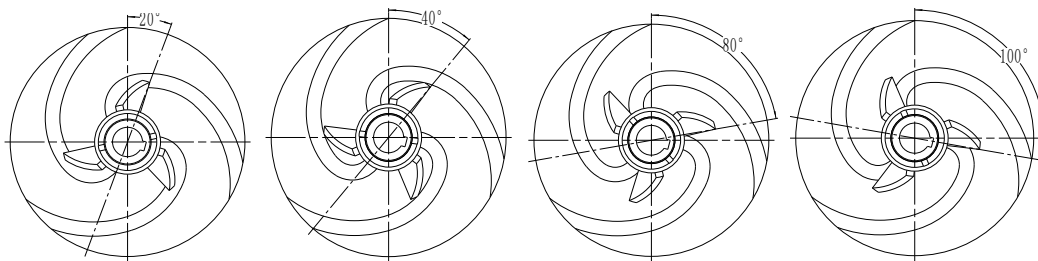


Figure 7. Schemes of 4 different relative angles.

### 3.1.2. Analysis of Internal Flow Field

The pressure distributions at different relative angles under  $1.0Q_{opt}$  flow rate are shown in Figure 8. The location of the comparison plane is the middle section of the volute, as shown the A-A interface plane in Figure 1. Although the pressure distributions at A-A plane is slightly different under different schemes, the overall changing rule is similar. The pressure increases gradually from the impeller inlet to the volute outlet along the main flow direction. The maximum value appears in the diffusion section of the volute, and the relative low-pressure area appears in the suction sides of the impeller near the blade inlet. With the increase in the relative angle between the rotary cutter and the impeller, the area of the relative low pressure gradually decreases. The relative high-pressure area in the volute and the diffusion section will gradually increase. When the angle is 100 degrees, the high-pressure area has occurred at the tongue. On the same section, the pressure at the volute inlet is obviously smaller than that at the volute outer wall, and the difference becomes obvious with the increase in the relative angle between the rotary cutter and the impeller.

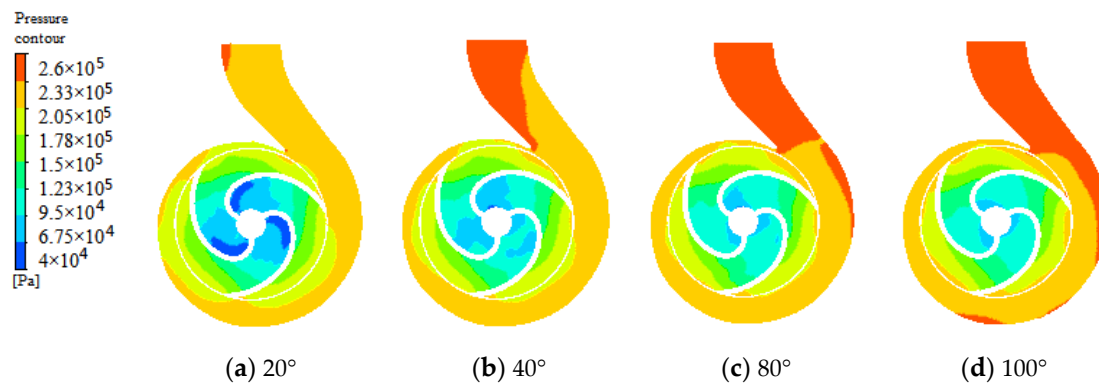


Figure 8. Pressure distributions under different relative angles.

Figure 9 is the distribution of relative velocity vector with four relative angles under  $1.0Q_{opt}$  flow rate in the plane of A-A. It can be obviously seen from the figure that there is a jet-wake structure in the upper right part of the impeller near the channel of the tongue, and velocity vector distributions in three flow channels are different.

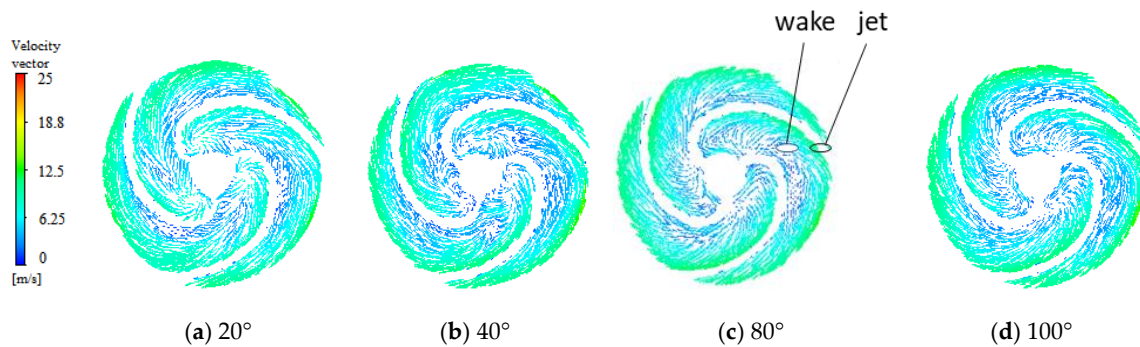


Figure 9. Velocity distributions under different relative angles.

The hydraulic loss depends on the velocity vector bandwidth. If the velocity vector width is smaller, the jet-wake structure is weaker, and the loss is smaller. It can be clearly seen from Figure 9 that when the relative angle of the rotary cutter and the impeller is 20 degrees, the velocity vector bandwidth is the smallest and the jet-wake structure is the weakest. With the increase in relative angle, the velocity vector bandwidth increases and the jet-wake structure becomes stronger. The scheme of relative angle between the rotary cutter and the impeller 20 degrees has been chosen for further research.

### 3.2. Time Aomain Analysis of Pressure Pulsation at Different Positions

In order to study the pressure fluctuation in the pump, dimensionless pressure pulsation coefficient  $C_p$  is defined as,

$$C_p = \frac{\Delta p}{\frac{1}{2}\rho u_2^2} \quad (1)$$

where  $\Delta p$  is the difference between the instantaneous pressure and the average pressure,  $p_a$ ;  $\rho$  is fluid density,  $\text{kg/m}^3$ ;  $u_2$  is the peripheral speed of the impeller outlet,  $\text{m/s}$ . Figure 10 is the time domain diagram of the pressure fluctuation at different locations under  $1.0Q_{opt}$  flow rate, the  $x$ -axis is the time, and it is dimensionless with the time required for one circle of the impeller,  $T = 0.0405405405$  s. When  $t/T = 0.125, 0.458$  and  $0.791$ , one blade just crosses the position of the tongue. When  $t/T = 0, 0.333, 0.666$ , a rotating cutter blade just aligns with the fixed cutter blades. By comparing the time domain of pressure fluctuation at different positions in Figure 10a, it is found that the amplitude of pressure fluctuation decreases from being near rotary parts to far away from them. The pressure fluctuation

amplitude at the lower plate (XP) is the largest, which is due to the double influence of impeller and rotary cutter at the lower plate. The pressure fluctuation amplitude in the clearance (Y) between the rotary cutter and the fixed cutter and the upper plate (SP) is relatively small. The inlet of the rotary cutter (JK) and the outlet of the volute (CK) are the farthest away from the rotating parts, thus pressure fluctuation is the smallest. From Figure 10b, it can be seen that the pressure fluctuation distributing at volute sections is regular, and pressure amplitudes decrease from the position near the tongue (G) to those far away from the tongue, followed by the first section (P1) near the tongue. This may be the result of the impeller and the rotary cutter simultaneous dynamic and static interference and overlapping with each other in the volute. In general, the pressure fluctuations of the lower plate (XP), the upper plate (SP) and the clearance between the rotary cutter and the fixed cutter (Y) are the most serious. The secondary peaks on the first section (P1) and the tongue (G) are more obvious, so these will be analyzed further.

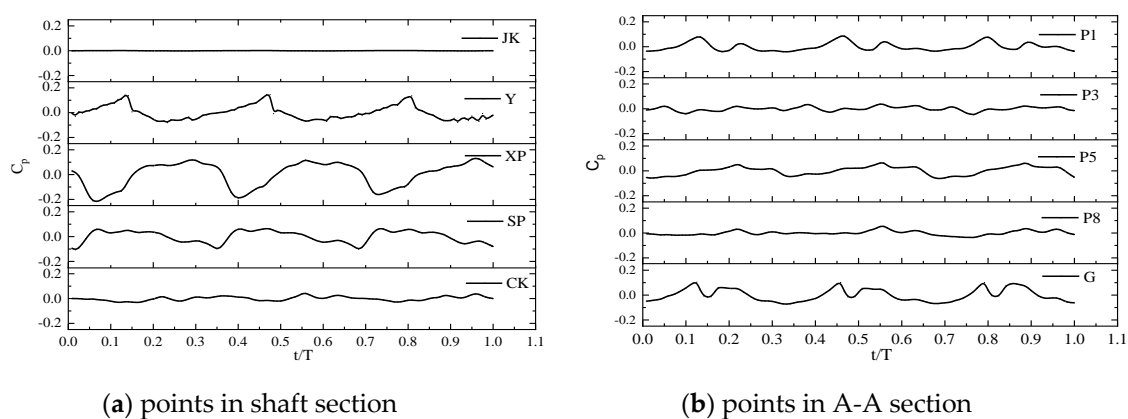


Figure 10. Pressure fluctuations for different locations.

Figure 11 shows the time domain of pressure fluctuations at the upper plate (SP), lower plate (XP), first section (P1), tongue (G) and the clearance between the rotary cutter and fixed cutter (Y) under different flow rates. It can be seen that the amplitude of pressure fluctuation at each monitoring point changes periodically, with three peaks and three valleys. This is the same as the number of impeller blades, but the amplitude at each monitoring point has a large difference under different flow rates. Under the condition of small flow rate, the amplitude is  $XP > SP > y > G > P1$ , under the  $1.0Q_{opt}$  flow rate,  $XP > Y > G > P1 > SP$ , and under the condition of large flow rate,  $XP > P1 > G > Y > SP$ . Overall, the maximum amplitude of pressure fluctuation appears at XP at different flow rates. This is because XP is between the rotary cutter and the impeller, which is affected by the double interference. In addition, there is an obvious time difference between wave peaks and wave valleys of each monitoring point, which is caused by the difference in relative positions of dynamic and static interactions.

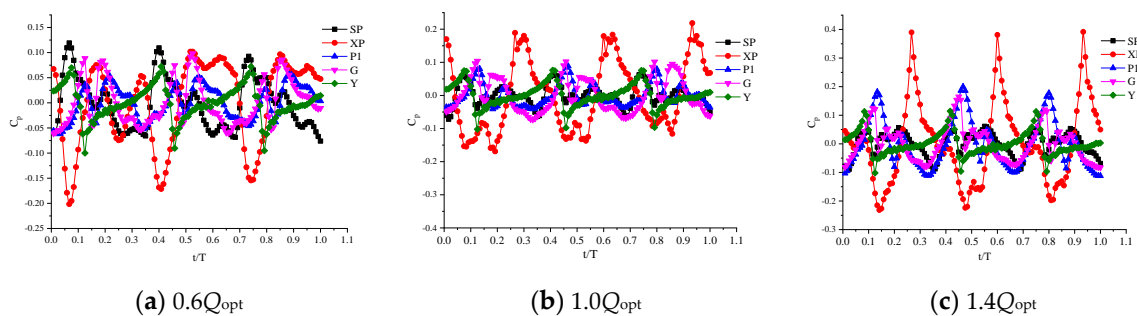


Figure 11. Pressure fluctuations under different flow rates.

Figure 12 shows the peak values in the time domain at the upper plate (SP), lower plate (XP), first section (P1), tongue (G), and the clearance between the rotary cutter and the fixed cutter (Y) at different flow rates. Except for SP, when the flow rate gradually increased from  $0.6Q_{opt}$  to  $1.4Q_{opt}$ , the wave peak and valley value of other four monitoring points all show an upward trend. Among them, P1 has the largest change, difference between the wave peak and valley has increased by 2.63 times. Change at Y is the smallest, from  $0.6Q_{opt}$  to  $1.4Q_{opt}$ , the value only increased by 1.25 times.

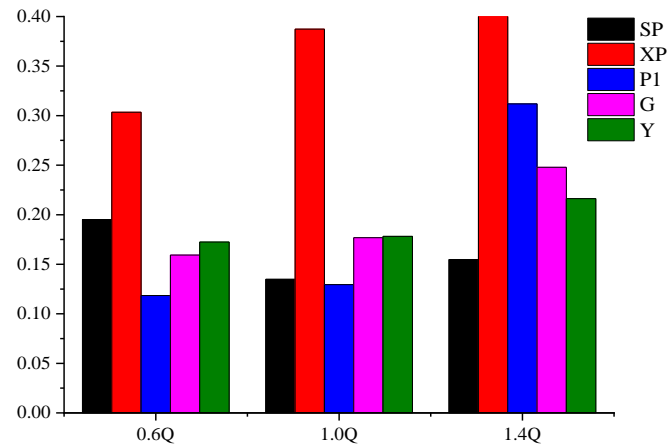


Figure 12. Difference between wave peak and valley under different flow rates.

### 3.3. Frequency Domain Analysis of Pressure Pulsation at Different Positions

The fast Fourier transform (FFT) is applied to the time domain signals of pressure fluctuation at each monitoring point, and the frequency domain of pressure fluctuation at the corresponding monitoring points is obtained. In this paper, when the impeller speed  $n$  is 1480 r/min, the shaft frequency  $f_n$  is 24.67 Hz, the number of impeller blades and rotary blades is three. The frequency of the impeller blade and the frequency of the rotary cutter blade are  $3f_n$ , which is 74.01 Hz. Under  $1.0Q_{opt}$  flow rate, the frequency domain is shown in Figure 13. It can be seen from the figure that the main frequency at each monitoring point is 74.01 Hz. The pressure fluctuation amplitude at frequency of  $3f_n$ , is the largest. In general, the pressure fluctuation frequency of each monitoring point is mainly concentrated within 0~600 Hz, and there are obvious low peaks in  $6f_n$ ,  $9f_n$ ,  $12f_n$ ,  $15f_n$ ,  $18f_n$ ,  $21f_n$ ,  $24f_n$ , etc. As the frequency increases, the peak value decreases until it nearly disappears. At XP point of the lower plate, the main frequency amplitude is much larger than other monitoring points, and the monitoring point Y at the clearance between the rotary cutter and the fixed cutter is the place with the largest number of frequency divisions.

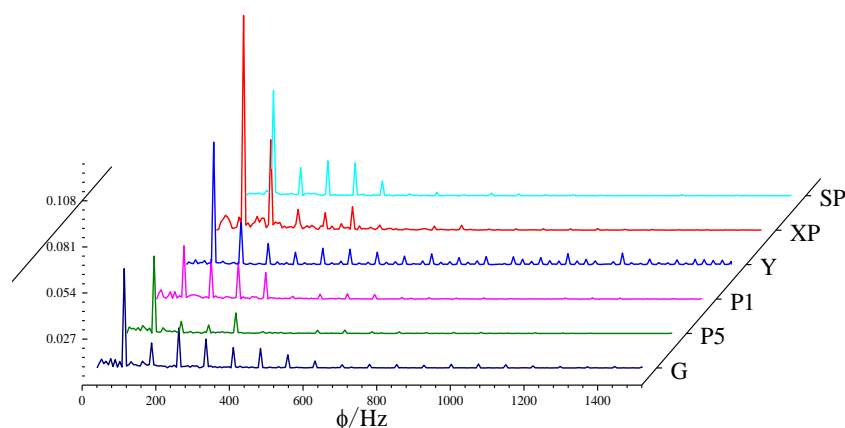
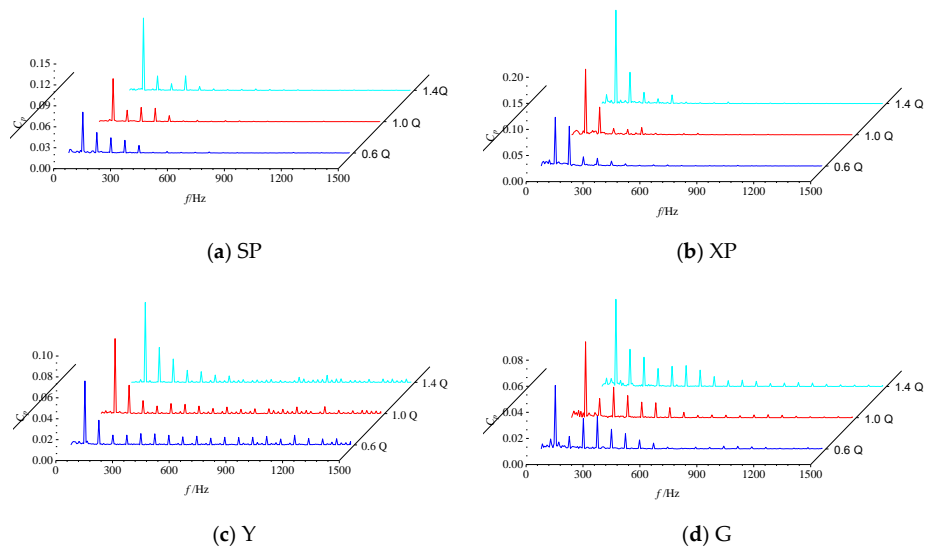


Figure 13. Frequency domains for different locations.

Figure 14 is the frequency domain of pressure fluctuation at the flow rate of  $0.6Q_{opt}$ ,  $1.0Q_{opt}$ , and  $1.2Q_{opt}$ , respectively, at the upper plate (SP), lower plate (XP), tongue (G) and the clearance (Y) between the rotary cutter and fixed cutter. It can be seen that the frequency characteristics of these four monitoring points are consistent with the changing rule of the pressure fluctuation amplitude. The main frequency of each monitoring point under different flow rates is always equal to the blade frequency. The pressure fluctuation amplitude of the four monitoring points is the smallest under the condition of  $0.6Q_{opt}$ . With the increase in the flow rate, the amplitude of pressure fluctuation at each monitoring point increases significantly and reaches the maximum value under  $1.4Q_{opt}$ . Therefore, it is necessary to avoid the operation of the cutting pump under the condition of large flow rate.



**Figure 14.** Frequency domains under different flow rates.

### 3.4. Analysis of Impeller Force

Figure 15 shows the radial force distribution on the pump impeller in one rotation period under the flow rates of  $0.6Q_{opt}$ ,  $0.8Q_{opt}$ ,  $1.0Q_{opt}$ ,  $1.2Q_{opt}$ , and  $1.4Q_{opt}$ . The radial force on the impeller changes with time as shown in Figure 15a with three peaks and three valleys, which are consistent with three impeller blades. Under  $0.6Q_{opt}$  flow rate, radial force on the impeller is the largest, with the peak value of 306 N. With the increase in the flow rate to  $0.8Q_{opt}$ ,  $1.0Q_{opt}$  and  $1.2Q_{opt}$ , radial force on the impeller gradually decreases, and the peak value under each flow rates is 274 N, 162 N and 87.3 N, respectively. Because of the complex interference of the internal flow field to radial force, there are obvious secondary peaks waves of radial forces except the largest peak. Figure 15b is the polar diagram of radial force on the impeller changing with rotation angle, where a rotation period of 360 degrees is selected. It can be seen from the figure that radial force changes with rotation angle, which is a periodic change of irregular clover petals. There are secondary peaks at 30 degrees, 150 degrees, and 270 degrees, lower peaks at 115 degrees, 225 degrees, and 345 degrees, and secondary valleys at many places.



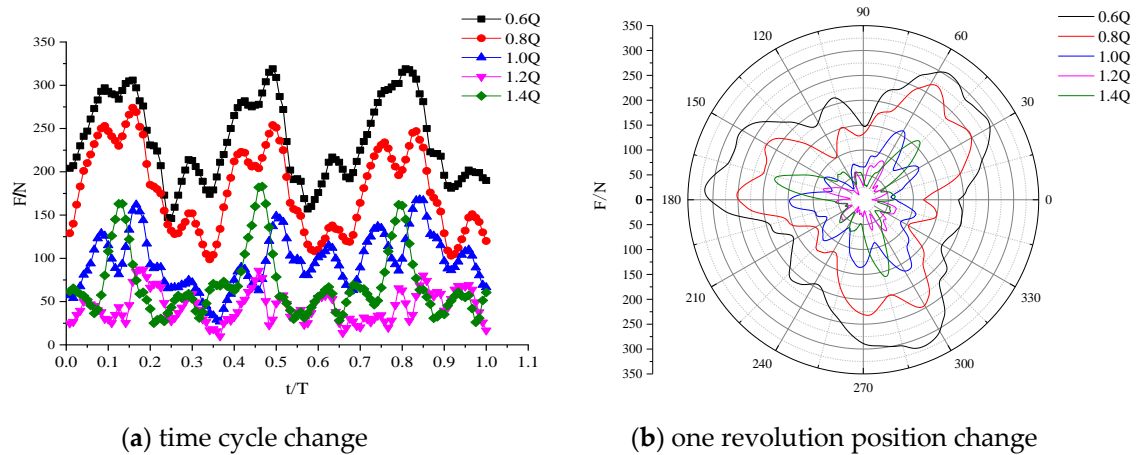


Figure 15. Radial forces on the impeller.

Figure 16 is the radial force vector of the pump impeller under the flow rates of  $0.6Q_{opt}$ ,  $1.0Q_{opt}$  and  $1.4Q_{opt}$ . The horizontal and vertical coordinates represent the components of radial force along X and Y axes, respectively. The number of sample points in each figure is 120 record points in one cycle. It can be seen from the figure that, at each flow rate, radial force on the impeller exhibits a triangular distribution, and its size and direction will change at any time. Under  $0.6Q_{opt}$  flow rate, radial force on the impeller is in the range of  $-280$  to  $300$  N in X axis direction, and in the range of  $-250$  to  $300$  N in Y axis direction. Under flow rate of  $1.0Q_{opt}$ , the radial force range of the impeller decreases, but the amplitude fluctuation increases; compared with small flow rate, the force distribution ranges of X axis and Y axis reduce to between  $-150$  and  $150$  N, that is to say, the radial force decreases significantly by nearly half. Under flow rate of  $1.4Q_{opt}$ , the radial force on impeller is similar to an irregular clover petal, and the periodicity is more obvious than the former two flow rates. Although there are three larger radial force peaks, more points concentrate at the center circle point where a smaller radial force is distributed.

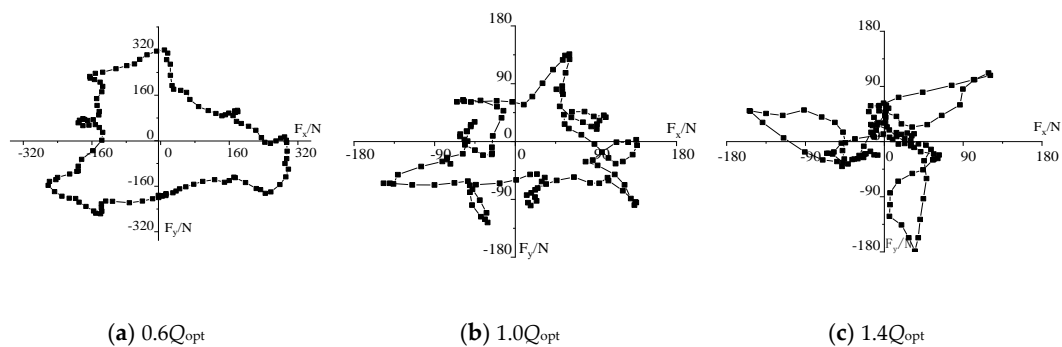


Figure 16. Vector of radial forces in impeller under different flow rates.

Figure 17 shows the axial force on impeller under flow rates of  $0.6Q_{opt}$ ,  $0.8Q_{opt}$ ,  $1.0Q_{opt}$ ,  $1.2Q_{opt}$ , and  $1.4Q_{opt}$ . Axial force on impeller changing with time is shown in Figure 16a, it changes periodically with time showing three peaks and three valleys. Compared with the radial force time distribution, the fluctuations are more regular and almost all sinusoidal curves have better stability. Under  $0.6Q_{opt}$  flow rate, the axial force on the impeller is the smallest, with a peak value of  $70.2$  N. As flow rate increases, axial force on the impeller gradually increases. The peak axial forces experienced by the impeller under  $0.8Q_{opt}$ ,  $1.0Q_{opt}$ ,  $1.2Q_{opt}$ , and  $1.4Q_{opt}$  flow rates are  $78.7$  N,  $98.3$  N,  $116$  N, and  $139$  N, respectively. In order to prevent the impeller from bearing large axial force and to extend the service life of the pump, it is necessary to avoid the pump running under the condition of large flow rate as much as possible. It can be seen from Figure 17b that, axial force changes with the rotation angle, showing

a periodic change of an irregular clover petal. When the impeller rotates to 90 degrees, 210 degrees and 330 degrees, there are obvious peaks. When the impeller rotates to 45 degrees, 165 degrees and 285 degrees, there are obvious valleys, as is consistent with the time domain of Figure 17a.

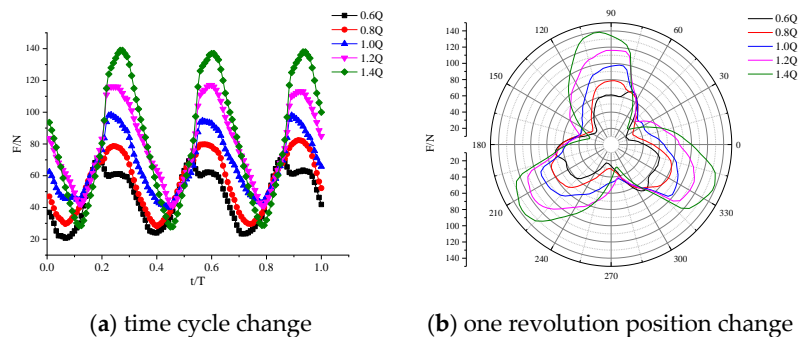


Figure 17. Axial force diagram of the impeller.

#### 4. Experiment

The external characteristics and pressure fluctuation test of the model pump are carried out on the multi-functional pump model test stand, and the layout of the test device is shown in Figure 18. The main instruments include semi-open submersible cutting pump, turbine flow-meter, flow regulating valve, outlet pressure transmitter, power distribution box, data acquisition instrument and so on.

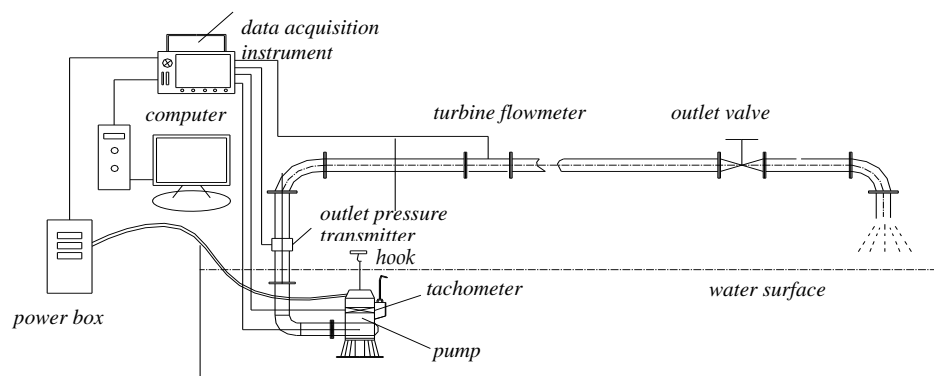
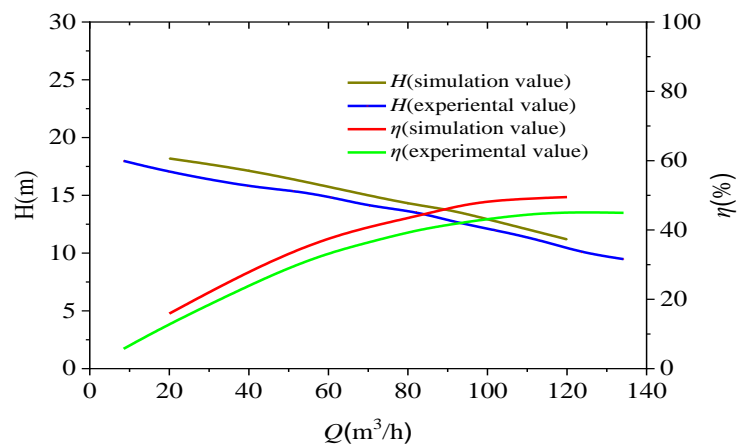


Figure 18. Layout of test bench.

The comparison of simulation curves and test curves of head and efficiency of the cutting pump under different flow rates is shown in Figure 19. The predicted results of numerical simulation are basically consistent with the test results. The simulation values of head and efficiency are larger than the test values, the head error is about 1.13 m, and the efficiency error is about 5%. Because of the selection of model, parameter, empirical formula, simplification of three-dimensional modeling and the technology of the pump in the process of simulation, there are some deviations between the simulation value and the test value. However, the trends are relatively consistent, so as to verify the reliability of this data calculation, suggesting that simulation can replace some tests for performance prediction.



**Figure 19.** Comparison of performance curves.

During the pressure fluctuation test, the flow rate is adjusted by adjusting the valve at the outlet of the pipeline. Through the outlet pressure transmitter, pump outlet pressure is obtained, and the electrical measurement method is used to measure and calculate the pump shaft power. The submersible high-frequency pressure sensor with an accuracy class of 0.25 and the measurement range of 0 to 1 MP<sub>a</sub> is used. The sampling frequency is 2960 Hz, and each sampling time lasts 20 s. The preliminary processing of data is completed by HSJ-2010 hydraulic machinery comprehensive tester (Huazhong University of science and technology, Wuhan, China). The main test instruments are shown in Figure 20.



**Figure 20.** Test instruments of pressure fluctuation.

The structure of the semi-open submersible cutting pump is compact and complex, so it is difficult for the sensor to insert deeply into the pump to measure the pressure distributions at upper and lower plates and other positions. Therefore, the pressure fluctuation sensors are installed at the volute section and outlet where the pressure fluctuations have a great influence on the sewage pumping process. The opening and tested position of volute is at Section III, V and VIII. The installation positions of the pressure fluctuation sensors are shown in Figure 21.



**Figure 21.** Test pump installed pressure sensors.

Figure 22 is the tested time domain of pressure fluctuations under flow rates of  $0.6Q_{opt}$ ,  $1.0Q_{opt}$  and  $1.4Q_{opt}$ . It can be seen that periodic fluctuations exist at the first section, the fifth section, the eighth section and the volute outlet, which is consistent with the simulation results. The number of peaks and valleys is 3 too, which is consistent with the number of blades. Under the condition of small flow rate, there are obvious secondary peaks at each monitoring point. As the flow rate increases, the amplitude of the pressure fluctuation at the monitoring point P1 further increases and is more obvious than those at other locations, which is consistent with the simulation. Under small flow rate, the waveforms of the fifth section, the eighth section and the volute outlet are more regular and clearer. However, as the flow rate increases, due to the internal high frequency sensor disturbing the internal flow field at cross sections, the waveform regularity at the volute outlet is significantly higher than those at other two positions, which is slightly different from the simulation. The setting of boundary conditions, the manufacturing process of test pump and its test environment leads to a certain gap between the simulation value and test value. But the fluctuation trend is relatively consistent on the whole.

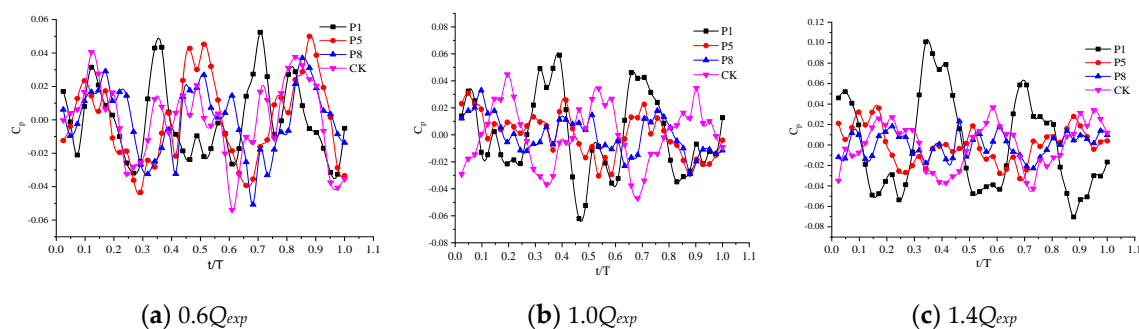


**Figure 22.** Comparison of pressure fluctuations under different flow rates.

Figure 23 shows the frequency domain comparison of pressure fluctuation at each monitoring point under different flow rates. It can be seen from the figure that, although there are some differences of the amplitudes results from simulation and experiment, their fluctuation trends are more consistent. The maximum peak appears at the three times axis frequency, indicating that the main frequency is the blade frequency, and there are obvious fluctuations at the blade frequency. In the low frequency area of each monitoring point under low flow rates, the frequency division components are more and their density is large. With the increase in the flow rate, the density and intensity of the frequency division of each monitoring point show a decreasing trend, and the simulation and test results are more consistent.

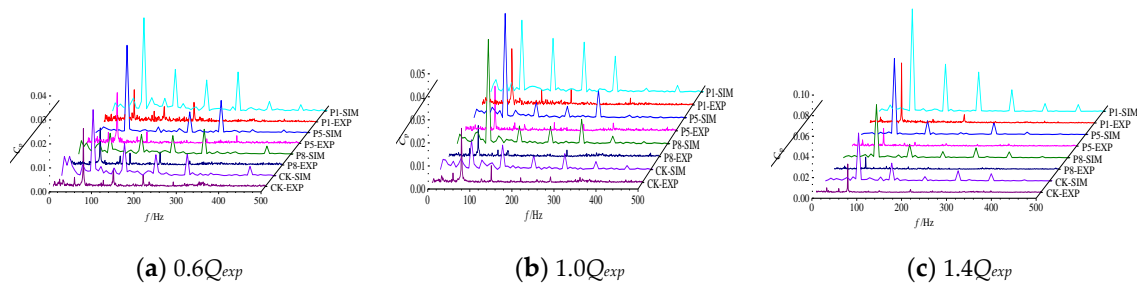


Figure 23. Comparison of frequency domains under different flow rates.

## 5. Conclusions

(1) The pressure fluctuation at each flow component shows a periodic change: the amplitude attenuates from a position near the rotating part to a position away from the rotating part, and from a position near the tongue to a position away from the tongue, and the fluctuation increases as the flow rate increases. Under different flow rates, the pressure fluctuation amplitude of lower plate XP is the largest, because the position is between the rotary cutter and the impeller, which is affected by the double interference.

(2) The pressure fluctuation main frequency is the blade passing frequency. In the low frequency region with multiple integrals of blade frequency and axial frequency, wave amplitudes are obvious, and in the high frequency region, wave amplitudes are weak. At each flow rate, the main frequency amplitude at the monitoring point of lower plate XP is much larger than those at other monitoring points. However, there are many low-frequency signals at the monitoring point Y between the rotary cutter and the fixed cutter, and the frequency components of the pressure fluctuation are complicated.

(3) The radial force and axial force on the impeller change periodically with time, and the number of peaks and valleys is consistent with the number of blades in one turn. Under different flow rates, the distributions of radial force and axial force show a strong similarity. The axial force experienced by the impeller increases with the increase in flow rate, while the radial force experienced by the impeller at flow rate of  $0.6Q_{opt}$  is the largest.

**Author Contributions:** W.C. designed and tested the scheme, and organized the paper. J.M. performed simulations, W.L. helped to analyze the data. All authors have read and agreed to the published version of the manuscript.

**Funding:** This work was supported by the National Key R&D Program of China (2018YFC0810506) and the Modern Agriculture Key R&D Program of Jiangsu (SBE2020310325).

**Conflicts of Interest:** The authors declared no potential conflicts of interest with respect to the research, authorship, and/or publication of this article.

## References

- Adkins, D.R.; Brennen, C.E. Analyses of hydrodynamic radial forces on centrifugal pump impellers. *ASME Trans. J. Fluids Eng.* **1988**, *110*, 20–28. [[CrossRef](#)]
- Barrio, R.; Fernández, J.; Blanco, E.; Parrondo, J. Estimation of radial load in centrifugal pumps using computational fluid dynamics. *Eur. J. Mech. B Fluids* **2011**, *30*, 316–324. [[CrossRef](#)]
- Yuan, S.; Zhou, J.; Yuan, J.; Zhang, J. Numerical simulation on radial hydraulic forces for screw-type centrifugal pump with splitter blade. *Trans. Chin. Soc. Agric. Mach.* **2012**, *43*, 37–42.
- González, J.; Santolaria, C.; Parrondo, J.L.; Fernández, J.; Blanco, E. Unsteady radial forces on the impeller of a centrifugal pump with radial gap variation. In Proceedings of the Joint Fluids Summer Engineering Conference, Honolulu, HI, USA, 6–10 July 2003; ASME/JSME: New York, NY, USA, 2003; pp. 1173–1181.
- Barrio, R.; Parrondo, J.; Blanco, E. Numerical analysis of the unsteady flow in the near-tongue region in a volute-type centrifugal pump for different operating points. *Comput. Fluids* **2010**, *39*, 859–870. [[CrossRef](#)]
- Solis, M.; Bakir, F.; Khelladi, S. Pressure fluctuations reduction in centrifugal pumps: Influence of impeller Geometry and Radial Gap. In Proceedings of the Fluids Engineering Division Summer Meeting, Vail, CO, USA, 2–6 August 2009; Volume 43727, pp. 253–265.

7. Van Esch, B.P.M. Performance and radial loading of a mixed-flow pump under non-uniform suction flow. *J. Fluids Eng.* **2009**, *131*, 0511011–0511017. [[CrossRef](#)]
8. González, J.; Parrondo, J.; Santolaria, C.; Blanco, E. Steady and unsteady radial forces for a centrifugal pump with impeller to tongue gap variation. *Trans. ASME* **2006**, *27*, 454–462. [[CrossRef](#)]
9. Wei, H.; Xuefeng, L.; Min, S.; Ting, Y.; Rennian, L.; Yi, J.; Lei, J.; Penglin, H. Pressure fluctuation of solid-liquid flow in stator and rotor cascades of pump as turbine. *J. Drain. Irrig. Mach. Eng.* **2018**, *36*, 99–103.
10. Weidong, C.; Lingjun, Y.; Qian, Z. Distribution of unsteady pressure in volute type axial flow pump. *J. Vibroeng.* **2018**, *188*, 1–11. [[CrossRef](#)]
11. Li, W.; Zhang, Y.; Sun, B.; Shi, W.; Xu, R. Rotor radial force and pressure fluctuation of the mixed flow pump under different flow conditions. *J. Drain. Irrig. Mach. Eng.* **2019**, *37*, 277–283.
12. Watson, C.; Wood, H.G. Optimizing a helical groove seal with grooves on both the rotor and stator surfaces. *Am. Soc. Mech. Eng.* **2017**, *50794*, V02BT41A044.
13. Obaidi, A.; Ramadhan, A.; Mohammed, A.A. Numerical investigations of transient flow characteristic in axial flow pump and pressure fluctuation analysis based on the CFD technique. *J. Eng. Sci. Technol. Rev.* **2019**, *12*, 70–79. [[CrossRef](#)]
14. Zhi, Z.; Yuan, Z.; Jieqing, J. Influence of wastewater mixer setting angle on flow field in sewage treatment pool. *J. Drain. Irrig. Mach. Eng.* **2020**, *383*, 272–276.



© 2020 by the authors. Licensee MDPI, Basel, Switzerland. This article is an open access article distributed under the terms and conditions of the Creative Commons Attribution (CC BY) license (<http://creativecommons.org/licenses/by/4.0/>).